Modeling ice block failure within drift ice and ice rubble

Malith Prasanna,[1,*] Arttu Polojärvi,[1] Mingdong Wei,[1] and Jan Åström[2]

[1]*Aalto University, School of Engineering, Department of Mechanical Engineering, P.O. Box 14100, FI-00076 Aalto, Finland*

[2]*CSC-IT-Center for Science, P.O. Box 405, FI-02101 Espoo, Finland*

(Received 25 November 2021; accepted 3 March 2022; published 14 April 2022)

A major challenge within material science is the proper modeling of force transmission through fragmenting materials under compression. A particularly demanding material is sea ice, which on small scales is an anisotropic material with quasibrittle characteristics under failure. Here we use the particle-based model HiDEM and laboratory-scale experiments on saline ice to develop a material model for fragmenting ice. The material behavior of the HiDEM model-ice, and the experiments are compatible on force transmission and fragmentation if: (i) the typical HiDEM glacier-scale particle size of meters is brought down to millimeters corresponding to the grain size of the laboratory ice, (ii) the often used HiDEM lattice structure is replaced by a planar random structure with an anisotropy in the direction normal to the randomized plane, and (iii) the instant tensile and bending failure criterion, used in HiDEM on glacier scale, is replaced by a cohesive softening failure potential for energy dissipation. The main outcomes of this exercise is that many of the, more or less, traditional ice modeling schemes are proven to be incomplete. In particular, local crushing of ice is not valid as a generic failure mode for fragmented ice under compression. Rather, shear failure, as described by Mohr-Coulomb theory is demonstrated to be the dominant failure mode.

DOI: 10.1103/PhysRevE.105.045001

I. INTRODUCTION

Material strength of ice has applications ranging from the mechanisms behind calving glaciers and ice shelves, to the triggering of avalanches and sea ice dynamics. Ice strength also controls drift-ice-induced damage on offshore structures and icebreaker functionality. Thick and more or less intact ice on large scales, e.g., glaciers, is often modeled as a high-viscous fluid governed by Glen's law [1]. For thinner ice, e.g., sea ice, purely viscous models are no longer very useful, in particular, when ice fragments and forms ice rubble.

Under compressive loading, ice often display quasibrittle behavior. Before reaching peak compressive stress, the stress-strain curve may deviate from linear. At peak-stress, failure occurs via crack propagation or shear band formation. When additional complexity of creep, plasticity, and viscoelasticity are added, it becomes evident that no general model is available to cover all aspects of the material behavior of sea ice [2]. In this investigation we focus on developing and improving material models for drift ice and ice rubble, which are basically granular materials consisting of floes and blocks of various sizes. The ice blocks within these materials interact through ice-to-ice contacts and they typically undergo a constant fragmentation process.

Compressive strength of granular material has been extensively investigated, and a central concept is *force chains* that transmit forces through networks of particles across compressive contacts [3]. The stability of the force chains determines their force-carrying capacity [4], and it has been shown that they often fail via geometrical buckling [5]. Paavilainen and Tuhkuri [6] and Ranta *et al.* [7] demonstrated this mechanism in ice rubble piles. When drift ice or ice rubble is densely packed, force chain buckling may become inhibited by confinement, and force chains may fail through fracture [8]. Compressive failure of ice has been studied extensively [9–11], and the failure mode has been noticed to depend on the loading rate, direction of the forces relative to the grain direction, and the confinement of ice blocks. In numerical modeling of sea ice, it has often been assumed that the local ice failure occurs due to crushing at contacts [12–14], even though it has remained unclear to what extent this is the dominating failure mechanism. In recent experiments by Prasanna *et al.* [15], it was demonstrated that the saline ice blocks fail predominantly by shear at compressive contacts. Shear strength of ice is a fraction of its compressive strength [11], and it appears that contacts transmit lower loads than predicted by local ice crushing.

The main objective of this investigation is to use the Bonded Particle Model (BPM) HiDEM [16–18] to reproduce the experiments of Prasanna *et al.* [15]. BPMs are often used to model the failure of complex materials, as a wide range of failure phenomena can be modeled via the interaction rules for the particles. Elastic-brittle material with instantaneous failure is the most straightforward to implement [19–22]. Viscoelasticity and creep can be introduced in a material by allowing particles to flow past each other and occasionally re-bond with neighboring particles [23,24]. Fatigue failure can be achieved by time incremental damage and healing of bonds [25,26], and bond failure criteria with material

[*]malith.prasanna@aalto.fi

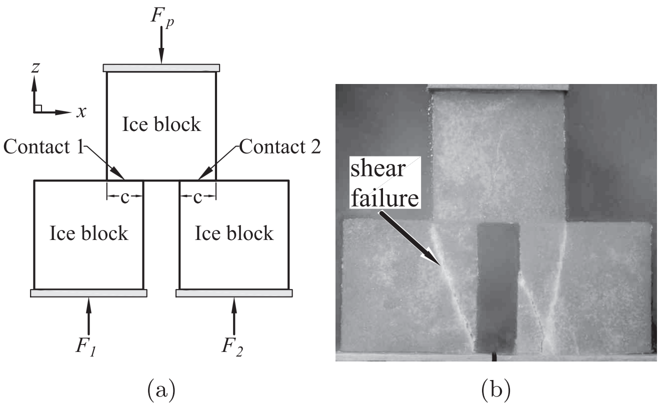

FIG. 1. (a) Illustration of the three-blocks system and (b) shear failure of the ice blocks.

softening can be used to obtain quasibrittle failure [27]. Coupling of mechanical and thermal responses is also possible in BPMs by varying the model parameters as a function of temperature [28]. Thus, BPMs are used widely to model sea-ice failure processes [29–32].

As will be demonstrated below, HiDEM can, to a large degree, reproduce the experiments of Prasanna *et al.* [15] with the following modifications: (i) the typical HiDEM glacier-scale particle-size of meters is brought down to millimeters corresponding to the width of the granular columns of the laboratory ice, (ii) the often used HiDEM lattice-structure is replaced by a planar random structure with an anisotropy consisting of granular columns in the direction normal to the randomized plane, and (iii) the instant tensile and bending failure criterion, used in HiDEM on glacier scale, is replaced by a cohesive softening failure potential with an efficient energy dissipation capability.

II. METHODS

Here we describe briefly the experiments of Prasanna *et al.* [15], the BPM-tool HiDEM including its modifications, the material model we used for mimicking the saline ice used in the experiments, and finally the parametrization of the computational model that produced the best match with the experiments.

A. Ice block breakage experiments

Figure 1(a) illustrates the setup of the ice block breakage experiments, which is described in detail in Prasanna *et al.* [15]. In the experiments, three 300 mm × 300 mm × 110 mm (length × width × thickness) ice blocks were set to form two ice-to-ice contacts. Compression was ramped up until failure occurred. The blocks were floating in saline water, thus, the ice was rather warm with the mean temperature of −2.5°C. The compressive force, F_p, and the force transmitted by each contact, F_1 and F_2, were recorded. The experiments were conducted using six contact lengths, $c = 25, 50, 75, 100, 125,$ and 150 mm. The ice blocks failed predominantly due to a strength of material type shear-band formation. Figure 1(b) shows lighter color bands, which correspond to vertically aligned failure planes reaching through the ice block thickness. The failure planes appeared to be similar to Coulombic shear faults, a common failure mechanism of ice under low confinement axial compression [33]. The key finding of these experiments was that the force transmitted by an ice-to-ice contact appeared to be limited by a bulk strength of material type failure rather than a failure caused by propagating cracks.

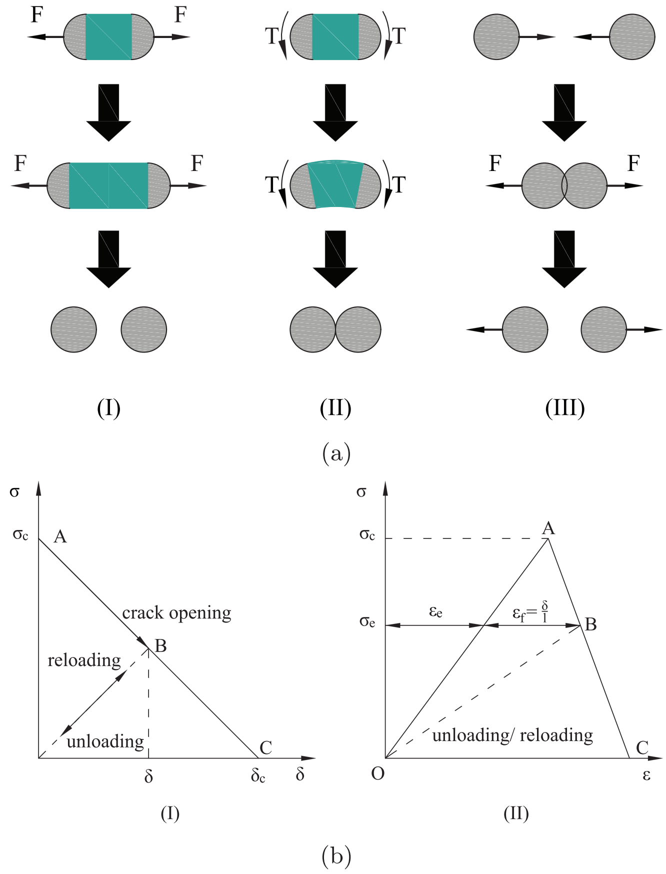

FIG. 2. (a) Adjacent particles are connected with beams which can fail (I) when a force F is applied or (II) when a moment T is applied. Further, particles that come into contact (III) will experience repulsive forces. (b) (I) Linear softening function of cohesive crack. (II) Stress-train response of a beam with cohesive crack. (Panels (a) and (b) reproduced from Åström *et al.* [17] and Paavilainen *et al.* [39], respectively.)

B. HiDEM

HiDEM models ice as a lattice of dense-packed spherical particles connected by Euler-Bernoulli beam elements. When beams break, microcracks form, which may combine to form larger cracks. Figures 2(a) (I) and (II) show illustrations of a beam element failing due to force applied or moment acting on particles. The equation of motion for particle i is [17]

$$\boldsymbol{M}\ddot{\boldsymbol{r}}_i + \boldsymbol{C}\dot{\boldsymbol{r}}_i + \sum_j \gamma_{ij}\boldsymbol{C}'\dot{\boldsymbol{r}}_{ij} + \sum_j \gamma'_{ij}\boldsymbol{K}\boldsymbol{r}_{ij} = \boldsymbol{F}_i. \quad (1)$$

Here $\boldsymbol{r}_i$ is the position vector of particle i and $\boldsymbol{r}_{ij}$ is its relative position vector with respect to particle j. $\boldsymbol{M}$ is the diagonal mass-matrix of the particle, while the matrix $\boldsymbol{C}$

contains damping coefficients for viscous drag. The matrix $\boldsymbol{C}'$ contains damping coefficients for the inelastic collisions between particles. The parameter γ_{ij} is unity for any particle pair i-j in contact and zero otherwise, while the parameter γ'_{ij} is unity for any particle pair i-j connected by a beam and zero otherwise. The matrix $\boldsymbol{K}$ is the stiffness matrix of the Euler-Bernoulli beams. $\boldsymbol{F}_i$ denotes the external forces acting on particle i. Equation (1) implies that an intact particle lattice exhibits granular viscoelastic material response: Elastic response due to initially linear-elastic response of Euler-Bernoulli beams (term $\boldsymbol{K}\boldsymbol{r}_{ij}$) and viscous response due to the damping (terms $\boldsymbol{C}\dot{\boldsymbol{r}}_i$ and $\boldsymbol{C}'\dot{\boldsymbol{r}}_{ij}$). In the standard HiDEM model, beams are set to fail instantaneously once their strains exceed a threshold value mimicking the formation of a brittle microcrack. Thus, it allows reproducing the general behavior of an elastic-brittle material and has been used extensively for investigating glacier calving, ice-shelf collapse, and sea-ice breakup [34–38]. When this model was applied to the three-block setup, it led to localized crushing at the contacts, and in some cases to shattering, caused by the instantaneous energy release from the failing beams. Such behavior was never observed in the experiments. Hence, it became evident that a failure model with material softening is required to capture the characteristics of the quasibrittle failure of millimeter scale saline ice. Softening dissipates the elastic energy stored in the beams, as the internal forces are ramped down to zero during the opening of a cohesive crack. For this purpose we implemented a cohesive softening model similar to that by Paavilainen *et al.* [39]. The model is based on the work of Hillerborg *et al.* [40] assuming that there is a cohesive zone in-front of and at the crack tip. When the crack propagates, the stresses in this cohesive zone do not instantaneously drop to zero, but decrease gradually as the crack opens. This results in dissipation of the elastic energy stored in the material, opposed to elastic waves caused by instantaneous beam failures that would shatter the material. The cohesive crack model used in this work assumes that the stress transferred through the cohesive crack is a linear function of crack opening displacement, δ. Figure 2(b) (I) presents the linear softening function used here.

In the cohesive softening model, a beam can only break via an intermediate cohesive crack forming at one of the ends of the beam. Each beam has three modes based on the status of the cohesive crack: linear-elastic mode, softening mode, and failed mode. In the linear-elastic mode, the beam is yet to reach the yield point, and the strains in the beam are governed by the Euler-Bernoulli beam theory. This behavior is presented in Fig. 2(b) (II) between points O and A. In the softening mode, a cohesive crack has formed and the strain in the beam is composed of an elastic and plastic part, ϵ_e and ϵ_f, respectively, in Fig. 2(b) (II). In the failed mode, the cohesive softening has ended and a true crack has formed, the beam does not transmit forces, and is considered broken [corresponds to the point C of Fig. 2(b) (II)]. In the cohesive mode, the tensile stress of the beam in its softening part, i.e., its outermost fiber, is calculated from

$$\sigma_t = E_b\left(\epsilon_t - \frac{\delta}{l}\right), \tag{2}$$

where σ_t is the tensile stress of the beam, E_b is the Young's modulus of the beam, δ is the crack opening displacement, l is the length of the beam in the undeformed configuration, and the term δ/l corresponds to the plastic strain due to the formation of the cohesive crack. Since the beams connect the centroids of the pairs of particles, l is simply the distance between them. ϵ_t is the total tensile strain at the out-most fiber, given by

$$\epsilon_t = \epsilon_a + \epsilon_l + \epsilon_r. \tag{3}$$

In this equation, ϵ_a, ϵ_l, and ϵ_r are the strains due to axial, lateral and rotational deformations, respectively. These strain components are calculated by using the shape function of the Euler-Bernoulli beam [41].

Here the failure criterion, F_c, for the cohesive crack is

$$F_c = \sigma_t - \sigma_c\left(1 - \frac{\delta}{\delta_c}\right), \tag{4}$$

where σ_c is the tensile strength of the beam material and δ_c is the critical crack opening displacement. When linear softening is assumed, δ_c is defined by using fracture energy, G_c, through

$$\delta_c = \frac{2G_c}{\sigma_c}\frac{\hat{l}}{\hat{l}^*}, \tag{5}$$

where $\hat{l}$ is the mean length of a beam in the lattice determined by summing the lengths of all the beams in a lattice and dividing by number of beams. $\hat{l}^*$ is a length scale calibration parameter for scaling δ_c for different particle sizes.

When a beam has an admissible stress state, i.e., $F_c < 0$ [Eq. (4)], it is in elastic mode, or the cohesive crack has formed and the beam is being loaded or unloaded [39] [as described in Fig. 2(b) (II) between points O and B]. The crack opens as $F_c \geqslant 0$, which in turn reduces the stresses in the beam. In this case an admissible tensile stress σ_e for the beam is calculated from

$$\sigma_e = \sigma_c\left(1 - \frac{\delta}{\delta_c}\right), \tag{6}$$

where

$$\delta = \frac{\epsilon_t - \dfrac{\sigma_c}{E_b}}{\dfrac{1}{l} - \dfrac{\sigma_c}{E_b\delta_c}}. \tag{7}$$

When the tensile stress reduces during the cohesive crack growth, the reaction forces and moments at the ends of the beam are scaled down proportionally to match the admissible stress state of the beam, effectively leading to behavior detected as material softening. It is important to note that even if the beams break under the tensile strains only, using the total strain of the beams [Eq. (3)] enables mixed mode failure; a beam connecting two spheres may break due to the relative translation and rotation of the spheres in any direction.

C. Microstructure ice model

Jirásek and Bažant [27] have shown that beam lattice topologies in BPM models have a significant bias on the failure paths. In regular lattices, such as square lattice or

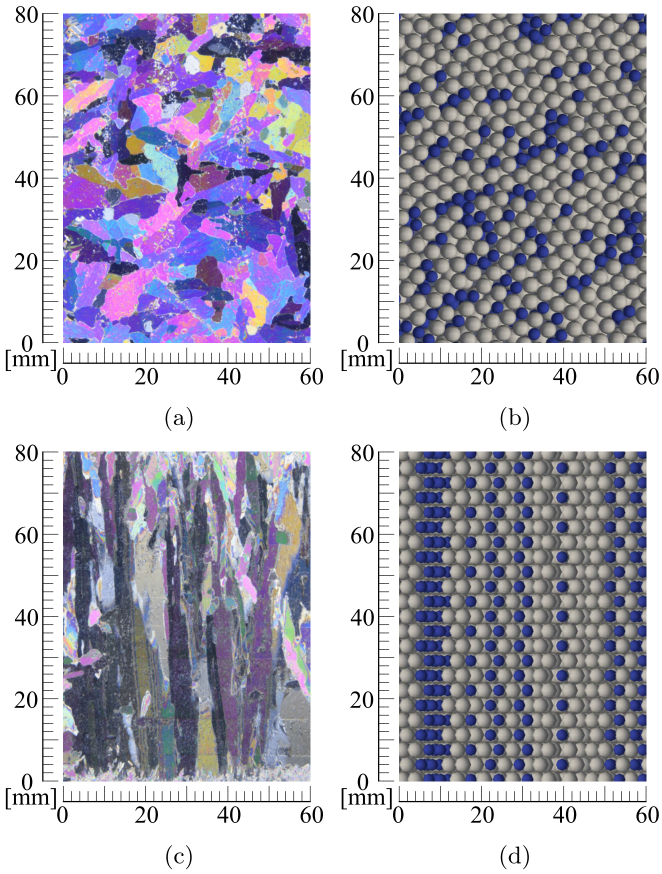

FIG. 3. Grain structure of ice compared to the AMSM model (a) Horizontal thin section of natural ice showing cross section of columnar grains. (b) Horizontal cross section of the AMSM model. (c) Vertical thin section of natural ice showing the columnar grains. (d) Vertical cross section of the AMSM model. On the right, blue (dark gray) and gray (light gray) particles have 1.5 and 2 mm radius, respectively.

hexagonal closed packed lattice, failure planes tend to align in the direction of principle or diagonal links. Therefore, a random lattice is required to minimize the influence of lattice topology on failure paths. Our preliminary simulations, however, with random lattices lead to numerous simultaneously occurring local failures with randomly oriented failure planes. This did not occur in the experiments, likely due to the grain structure of the saline ice specimens tested. The ice in the experiments resembled naturally grown ice, usually having a vertically aligned columnar grained microstructure, with the grains aligned parallel to the direction of ice growth [42]. The columnar grain structure of the ice used in the breakage experiments is illustrated by the horizontal and vertical thin sections of Figs. 3(a) and 3(c), respectively. Due to its microstructure, natural ice is an anisotropic material with different mechanical properties in horizontal and vertical directions [11]. Young's modulus, the tensile strength and the compressive strength are, respectively, about 1.2, 3, and 4 times higher in the direction along the columnar grains [42]. Moreover, the failure modes and the underlying failure mechanisms depend on the direction of loading with respect to the grain direction [9]. Therefore, we introduced an anisotropic

TABLE I. Model parameters.

Model parameter	Value	Unit
Beam width (w_b)	2	mm
Young's modulus of the beams (E_b)	600	MPa
Tensile strength of the beams (σ_c)	6	MPa
Energy absorbed by the cohesive crack (G_c)	600	Jm^{-2}

microstructure model (AMSM) to replicate the grain structure of the ice used in the experiments.

The modeled ice specimens were generated as follows. First, a 2D model was used to deposit circular elements in to a square shaped box replicating the horizontal cross section of columnar ice. A radii distribution of 70% 2 mm and 30% 1.5 mm was used. Then the circles were converted to spheres to form a planar random lattice seen in Fig. 3(b). Finally, this lattice was replicated in the vertical direction in a hexagonal closed packing to generate the microstructure of ice. Figure 3(d) presents the vertical cross section of the AMSM showing the columnar arrangement. Initially, a large ice block of 1200 mm × 1200 mm × 110 mm was created and smaller ice blocks were sampled from that. The blocks were sampled close to the center of the large ice block to minimize the effects of walls in the model. In the simulations below, ice specimens were loaded perpendicular to the columnar grain direction similarly to the experiments. Each three-block system modeled contain about 6×10^5 particles.

D. Parametrization of the model

Parametrization is one of the challenges related to BPM simulations. Techniques for calibrating models for isotropic materials exist [43,44], but due to the anisotropy of the ice and the AMSM topology used, these could not be utilized here. Parametrization was instead, performed by simulating uniaxial compressive failure experiments on single ice blocks. A similar setup was also used in the experiments. The model was calibrated to replicate the experimental stress-strain curves, strain and stress at failure, and the observed failure patterns of the block.

During parameter testing it became evident that the beam width, w_b, is one of the key parameters, since it affects the response of the beams in both the elastic and the softening modes. With w_b fixed, the desired macroscopic elastic modulus of the ice could be adjusted by setting the elastic modulus of the beams, E_b. Optimal material behavior was achieved with $w_b = r_{\max}$, where $r_{\max}$ is the largest particle radius. Another key parameter is the tensile strength of the beams, σ_c, which controls the macroscopic strength of the modeled specimens. Neither the failure patterns nor the general shape of the stress-strain curves changed significantly with σ_c, thus, its value was simply set to match the compressive strength of the experiments. The fracture energy absorbed by the cohesive crack, G_c, influenced the macroscopic behavior of the material at failure. Increasing the value of G_c from zero changed the shattering behavior into shearlike failure patterns that closely resembled the experiments. Table I summarizes the model parameters used in the simulations.

TABLE II. Bulk material properties of the AMSM lattice used in HiDEM simulations. Corresponding experimental values are in parentheses.

Property	Across columns	Along columns	Unit
Young's modulus	108 (130)	144	MPa
Tensile strength	476	1059	kPa
Compressive strength	1018 (820)	2703	kPa

It is important to notice that the parameter values presented in Table I are input values for the HiDEM model. The actual material properties of the model ice were obtained from numerical experiments. Table II presents the bulk material properties of the AMSM lattice used here, together with the values of Young's modulus and the compressive strength of the saline ice used in the experiments.

III. RESULTS

A. Three-block breakage experiment simulations

Having developed a working saline-ice model for HiDEM, we simulated the three-block breakage experiments [Fig. 1(a)] for all contact lengths used in the experiments. Six simulations were conducted for each c by using six different sphere packings in order to account for the potential scatter in simulation results. Figure 4 presents typical failure patterns from the simulations for each c. As apparent from the figures, the three-block setup failed typically via shear zones pinpointed to contact margins. The failure first occurred at one of the contacts, predominantly due to shear faulting. The failure patterns obtained from the simulations are in good agreement with the failure patterns observed in the experiments (Prasanna *et al.* [15], Fig. 9), where about 75% of the specimens failed due to shear. The analysis focused on the first contact to fail,

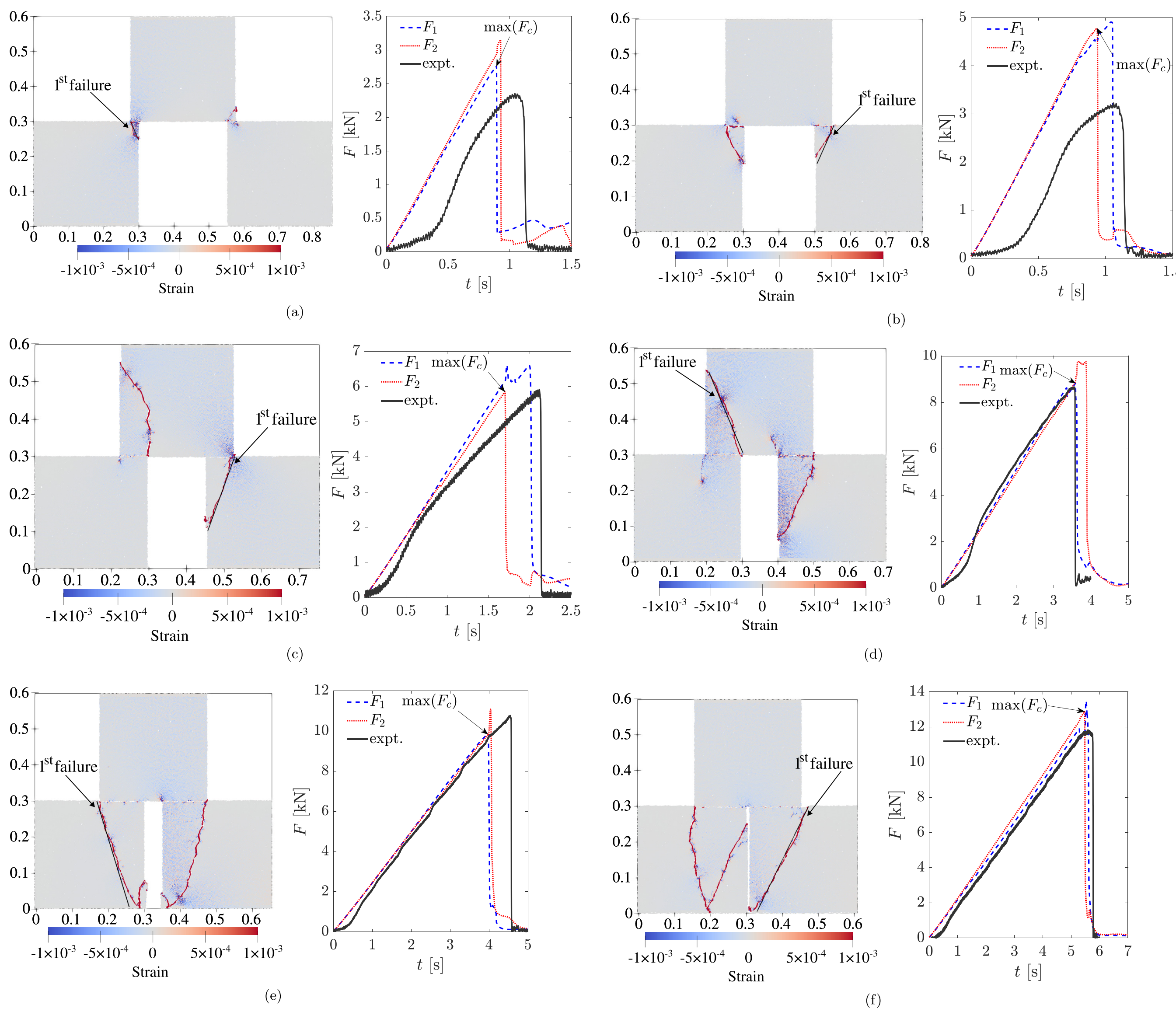

FIG. 4. Failure patterns and F-t curves of three block breakage experiment simulations: (a) c = 25 mm, (b) c = 50 mm, (c) c = 75 mm, (d) c = 100 mm, (e) c = 125 mm, and (f) c = 150 mm. The black line (dark straight line) in failure pattern figures are failure planes predicted by using Mohr-Coulomb failure criterion as explained in Sec. III B.

since immediately after the first failure the second contact failed as the loading conditions changed and the total compressive force was transmitted through the second contact. The shear faults could be identified by the relatively straight failure path with 20°–30° angle with respect to the direction of the compressive force and a failure plane parallel to the direction of columnar grains [45]. In contrast, typical shear crack driven by stress concentration could be identified by a parabolic failure-path, which curves towards a free edge of the specimen [46].

Figure 4 further compares the force versus time (F-t) curves from the simulations and the experiments. Forces transmitted by both contacts, F_1 and F_2 [Fig. 1(a)], are displayed. For computational reasons the compression time in the simulations, t_{sim}, was much shorter than in the experiments. Time in the simulations is therefore rescaled to match the experimental time, t_{expt}, via the equation

$$t = t_{\text{sim}} \frac{\dot{\epsilon}_{\text{sim}}}{\dot{\epsilon}_{\text{expt}}}. \tag{8}$$

Furthermore, for technical reasons, the simulations were performed with displacement controlled, while the experiments were force controlled. In Eq. (8), $\dot{\epsilon}_{\text{sim}}$ and $\dot{\epsilon}_{\text{expt}}$ are the strain rates in the simulations and the experiments, respectively. In the experiments, $\dot{\epsilon}_{\text{expt}} = 2.0 \times 10^{-3}$ s^{-1}, while in the simulations $\dot{\epsilon}_{\text{sim}} = 6.7 \times 10^{-3}$ s^{-1}.

The simulated F-t curves are similar to the experimental curves, except for the cases with $c = 25$ and 50 mm. The maximum contact force transmitted by the first contact to fail, $\max(F_c)$, increases with the contact length. The nonlinear initial part for the small c in the experiments is due to an initial misalignment of the blocks and consequent ice blocks settling at the contacts. Simulations, as expected, do not show this. As c increases, the significance of the misalignments decreases. For the larger c values, $c > 50$ mm, the simulations mimic the F-t behavior and the failure patterns well. The nonlinearity close to the peak in the experimental F-t curve is due to the formation of microcracks and partly inelastic (plastic, creep) deformations along the failure planes at the contacts. The simulated F-t curves display less nonlinear behavior near the peak, even if the simulated shear failure patterns otherwise indicate quasibrittle failure. In the simulations, microcracking along the failure planes is captured by the model, but all forms of inelastic deformations are not included. The prepeak difference between simulations and experiments is, thus, not very surprising.

For shear failure, critical shear force, F_τ, and critical normal force, F_n, acting on the shear plane [Fig. 5(a)] can be, respectively, calculated as

$$F_\tau = \max(F_c) \cdot \cos(\theta), \tag{9}$$

$$F_n = \max(F_c) \cdot \sin(\theta), \tag{10}$$

where $\max(F_c)$ is the maximum contact force and θ is the angle between the shear plane and the loading direction. The length of the shear plane can be estimated by fitting a straight line along the plane. The area of the shear plane, A_τ, is approximately the shear plane length multiplied by the thickness of the ice block.

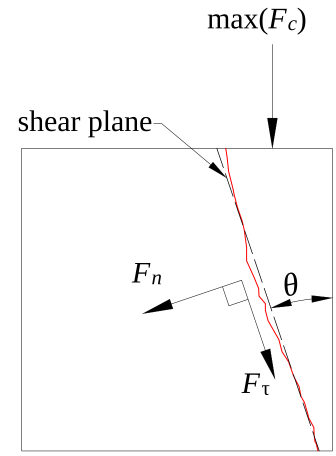

(a)

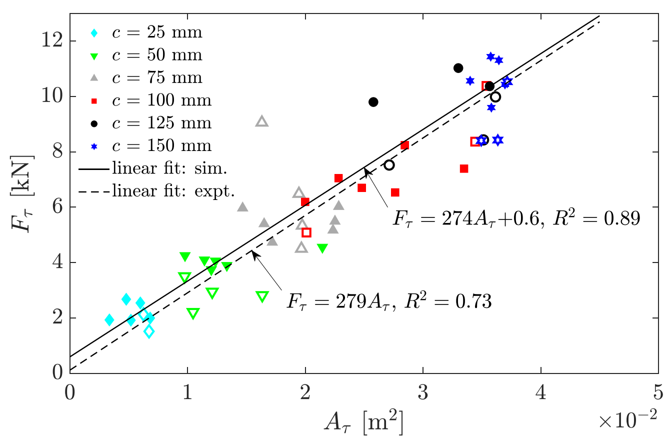

(b)

FIG. 5. (a) Critical shear force, F_τ, and critical normal force, F_n, acting on a shear plane. (b) F_τ plotted against area of failure plane, A_τ. Simulation and experiment results are marked with closed and open markers, respectively.

Figure 5(b) shows F_τ plotted against A_τ in the simulations and the experiments. The figure also shows fitted trend lines for both data sets. The simulated and experimental results agree well, there is relatively small scatter in the data, and there is an apparent linear dependency between the values of F_τ and A_τ. This suggests that the failure was governed by the bulk strength of the material, in contrast to shear crack propagation induced by stress concentration, which should lead to a significantly larger scatter in the data, and not a clear linear relation between F_τ and A_τ. Moreover, it is important to note that the data points corresponding to different contact lengths are mixed, which confirms that the trend in the plot is not an artifact related to the geometry of the three-block setup.

The very slight deviation in trend lines of Fig. 5(b) is partly due to the strain rate in the simulations being about 1.5–5.0 times higher than in the experiments. The computational strain rates had to be increased to achieve reasonable simulation times. Preliminary simulations with the strain rates up to 40 times higher than in the experiments yielded similar linear trend, but with a higher intercept.

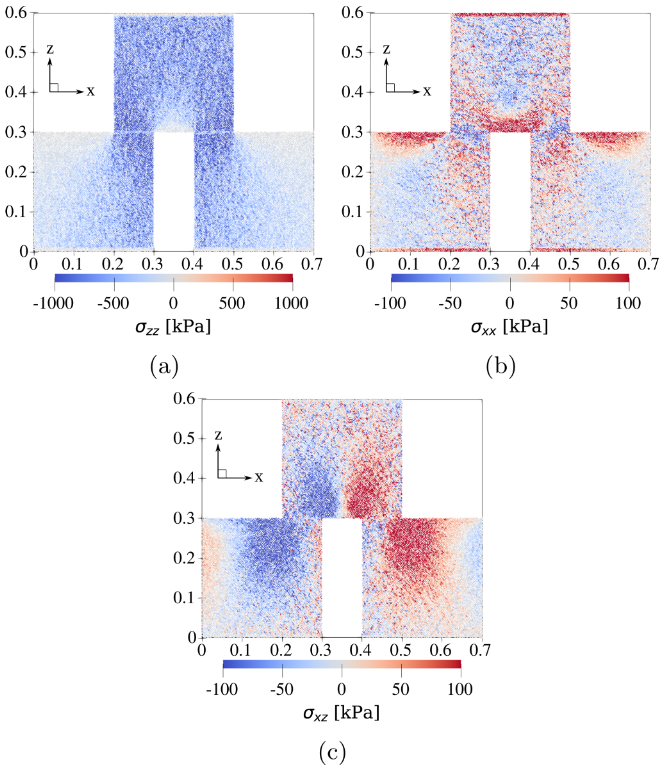

FIG. 6. Stress distribution in three-block system: (a) σ_{zz}, (b) σ_{xx}, and (c) σ_{xz}. Contact length $c = 100$ mm.

B. Ice failure mechanisms

The results above suggest that ice failure can be explained by using prefailure stress distributions and bulk strength of the material. For this purpose we need to compute the Cauchy stress tensor, $\boldsymbol{\sigma}_i$, which for particle i can be calculated using [47]

$$\boldsymbol{\sigma}_i = \frac{1}{2\Omega_i}\left(\frac{1}{2}\sum_j \mathbf{r}_{ij}\otimes\mathbf{f}_{ij} + \mathbf{f}_{ij}\otimes\mathbf{r}_{ij}\right), \qquad (11)$$

where Ω_i is the volume of particle i, $\mathbf{f}_{ij}$ is the force on i due to the beam connecting it to particle j, $\mathbf{r}_{ij}$ is the position vector of particle j with respect to particle i, and $\otimes$ is the tensor product between the two vectors.

Figure 6 shows the stress distribution of the three block system in the $c = 100$ mm case just before the failure plane begins to form. The figure shows that σ_{zz}, with its direction aligned with the load, is the dominant stress component. Also a zone of high shear stress, σ_{xz}, exists near the edge of the contacts. All of these stresses are largely uniform in the y direction.

The observed prefailure stress distributions and failure patterns show characteristics of Coulombic shear faults [48], which makes the Mohr-Coulomb failure criterion a natural hypothesis. According to this criterion, failure occurs when

$$\tau_0 = |\tau| - \mu\sigma_n, \qquad (12)$$

where the material properties τ_0 and μ are the internal cohesion and the internal friction and, τ and σ_n are the shear and normal stresses on a failure plane, respectively. The directions of τ and σ_n are the same as the directions of F_τ and F_n in Fig. 5(a).

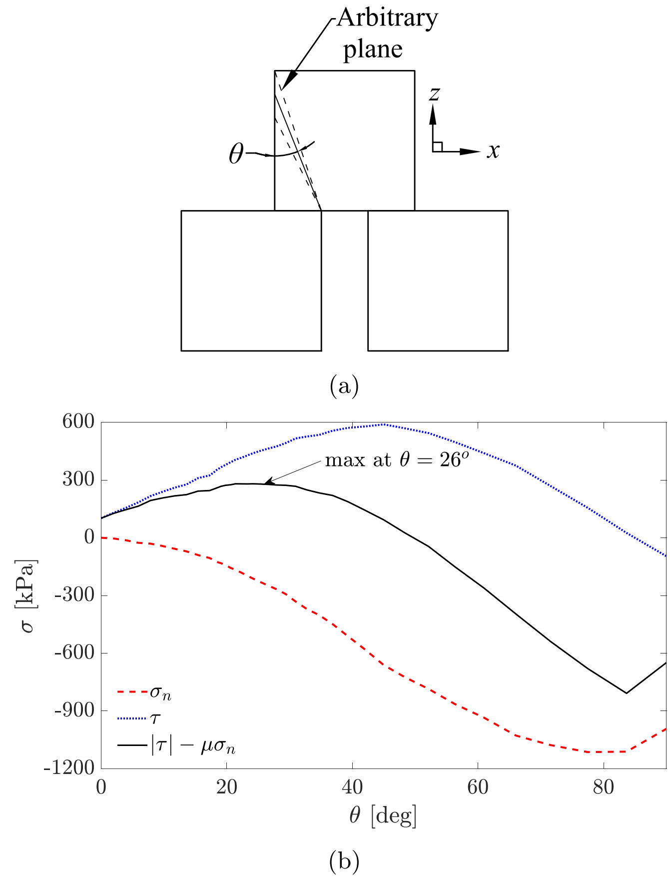

FIG. 7. (a) Plausible shear failure planes for arbitrary θ values. (b) Mohr-Coulomb failure criterion applied to $c = 100$ mm contact simulation of Fig. 6. Stress components of Mohr-Coulomb failure criterion vs θ.

The failure patterns (Fig. 4) showed that it is justified to assume that the shear planes go through the edges of the contacts. Thus, to confirm the Mohr-Coulomb theory, the only missing piece is that the failure plane should have an orientation that corresponds to the plane with the maximum average value for $|\tau| - \mu\sigma_n$. The stresses acting on a plane having an angle θ [Fig. 7(a)] can be solved from

$$\sigma_n = \tfrac{1}{2}(\sigma_{xx} + \sigma_{zz}) - \tfrac{1}{2}(\sigma_{xx} - \sigma_{zz})\cos 2\theta - \sigma_{xz}\sin 2\theta \qquad (13)$$

and

$$\tau = -\tfrac{1}{2}(\sigma_{xx} - \sigma_{zz})\sin 2\theta + \sigma_{xz}\cos 2\theta. \qquad (14)$$

The right side of Eq. (12) can, thus, be calculated for arbitrary values of θ. Figure 7(b) shows τ, σ_n, and $|\tau| - \mu\sigma_n$ with $\mu = 0.75$ as a function of θ. Here the average value of each stress component acting on a plane with given θ was used. Figure 7(b) shows that the maximum value for $|\tau| - \mu\sigma_n$ appears at $\theta = 26^\circ$. The directions of the simulated failure planes, presented in Fig. 4(d), match well with this. The maximum value of the failure criterion, 280 kPa, corresponds to τ_0. Figure 7(b) also shows that the maximum τ occurs around $\theta \approx 45^\circ$, which would be the failure plane angle if

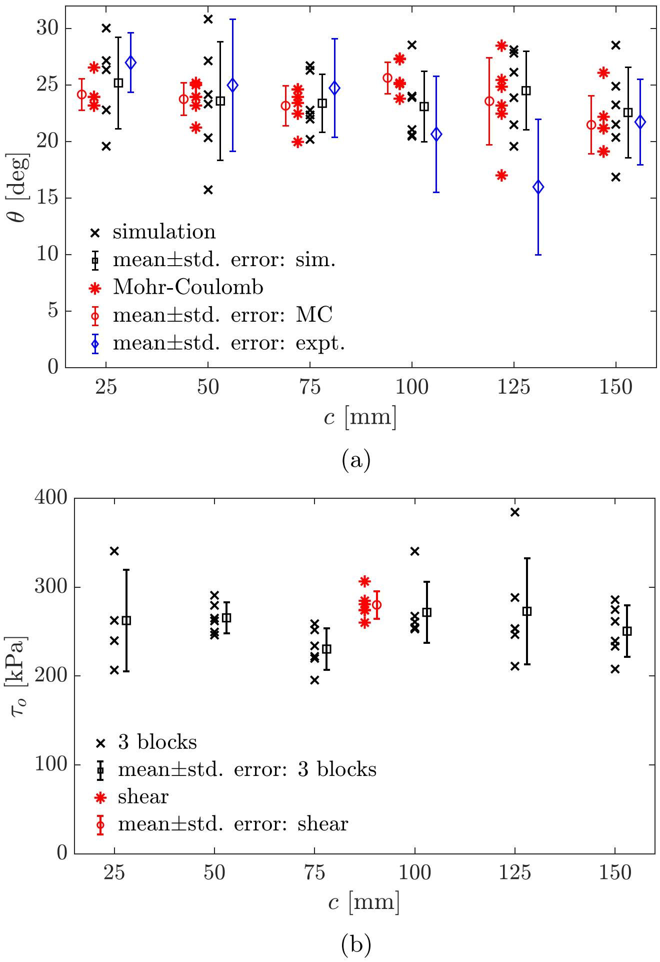

FIG. 8. (a) Failure plane angles, θ, calculated using Mohr-Coulomb failure model and from the simulations. (b) Values of internal cohesion, τ_0, calculated using Mohr-Coulomb failure model.

the Rankine failure criterion would have been the correct one. This further supports the Mohr-Coulomb failure criterion.

Similar analyses were conducted for all simulated failure planes and Fig. 8(a) shows that the values of θ obtained from the Mohr-Coulomb model compare well with the values of θ in the simulations. The figure also includes the mean values and the standard deviations of θ from the experiments. Mean values of θ are all similar and the standard deviations overlap. Further, the black lines in Fig. 4 show the Mohr-Coulomb failure planes and demonstrate that they compare well with the ones in the simulations. θ is approximately constant for all c, which is an important observation for further modeling. Figure 8(b) shows the values for internal cohesion, τ_0, obtained from the Mohr-Coulomb model [Eq. (12)] plotted against c. The figure also shows τ_0 calculated from simulations of single ice block failed under pure shear. While τ_0 data shows some scatter, the mean values and the standard deviations for all c are similar; τ_0 is approximately constant for all simulations as it should be, given it is a material property. The τ_0 values are also in agreement with the corresponding values measured in Couette-experiments on fresh water ice by Weiss *et al.* [49] as well as estimates of τ_0 obtained by extrapolating the post terminal compressive stress plots for onset of sliding across Coulombic shear faults in fresh water ice [50].

To finalize the results needed for outlining a material model for drift ice, we conducted a length-scale analysis with single-block simulations in two different ways [51]: (i) we scaled up the block-size by increasing the sizes of beams and particles, and (ii) we used constant beam and particle sizes and modified the size of the block by adding more particles and beams. As expected, with a dimensionless softening failure, the stress-strain behavior remained independent of size in the first case. In the second case, we observed moderate weakening with increasing block size, which is also expected [52]. No other significant material behavior changes with size was observed. This size analysis was however limited to less than an order of magnitude in linear size for computational reasons.

IV. DISCUSSION

We have investigated the use of the BPM-tool HiDEM to model quasibrittle failure of columnar grained, saline, ice in compressive ice-to-ice contacts by simulating the three-block breakage experiments of Prasanna *et al.* [15]. Based on the study, it is possible to highlight three key requirements for BPM models used for simulating the compressive failure of sea ice. First and foremost, a failure criterion with cohesive softening is needed to capture the quasibrittle failure behavior of ice. Saline ice, and especially warm sea ice floating in water, can not be modeled without a strong dissipation of elastic energy during fracture.

Second, a mixed-mode failure criterion is essential to capture the Coulombic shear faulting in simulations. The ice strength and the failure mode is set by the Mohr-Coulomb theory and the failure criterion need to contain both shear and normal stress components. Even though the Mohr-Coulomb theory essentially predict scale invariant fracture, a moderate weakening with size is expected. We have here demonstrated the validity of our model for engineering scale (~1 m) ice blocks, and it has been suggested that Coulombic shear faulting also occur at geophysical scales (~100 km) [9,53]. It still remains unclear, however, to how large sizes our BPM could be scaled up before it would no longer capture the essential physics of sea ice fracture. At geophysical scale, in particular, the parametrization would likely change significantly.

The third key point is that a AMSM topology models columnar grained ice better than random or structured lattices. Here it became apparent that the grain structure has to be replicated in BPM model lattices to achieve realistic failure planes. This has implications for BPM simulations of sea ice at larger scales than the mm-scale used here. It may be reasonable to model sea ice using particles as large as the thickness of the ice. This is possible because failure occurs predominantly along vertical planes that cut through the entire thickness of the ice.

To summarize, a BPM for drift ice should contain a mixed-mode softening failure potential to dissipate energy at ice failure, and when the particle and beam sizes are scaled up from the mm-scale, the anisotropy of the ice and the scale dependence of ice strength should be taken into account. With these additions, BPMs for drift ice, at the meter scale and below, should improve significantly, even though some aspects, like viscoelasticity and a full description of plasticity are still missing from the model.

ACKNOWLEDGMENTS

The authors are grateful for the financial support from the Academy of Finland through Project No. 309830, Ice Block Breakage: Experiments and Simulations (ICEBES). The authors acknowledge CSC–IT Center for Science, Finland, for computational resources under Project No. 2000971, Mechanics and Fracture of Ice.

[1] R. Greve and H. Blatter, *Dynamics of Ice Sheets and Glaciers*, Advances in Geophysical and Environmental Mechanics and Mathematics (Springer, Berlin, 2009).
[2] V. Dansereau, J. Weiss, P. Saramito, and P. Lattes, Cryosphere **10**, 1339 (2016).
[3] J. F. Peters, M. Muthuswamy, J. Wibowo, and A. Tordesillas, Phys. Rev. E **72**, 041307 (2005).
[4] A. Tordesillas, D. M. Walker, and Q. Lin, Phys. Rev. E **81**, 011302 (2010).
[5] A. Tordesillas, Philos. Mag. **87**, 4987 (2007).
[6] J. Paavilainen and J. Tuhkuri, Cold Reg. Sci. Technol. **85**, 157 (2013).
[7] J. Ranta, A. Polojärvi, and J. Tuhkuri, Cold Reg. Sci. Technol. **147**, 34 (2018).
[8] A. Pustogvar, A. Polojärvi, K. V. Høyland, and I. M. Bueide, in *Proceedings of the International Conference on Offshore Mechanics and Arctic Engineering - OMAE* (Elsevier, 2014), Vol. 10, p. V010T07A023.
[9] E. Schulson, Eng. Fract. Mech. **68**, 1839 (2001).
[10] E. M. Schulson and P. Duval, *Creep and Fracture of Ice* (Cambridge University Press, Cambridge, UK, 2009).
[11] G. Timco and W. Weeks, Cold Reg. Sci. Technol. **60**, 107 (2010).
[12] M. A. Hopkins and W. D. Hibler, Ann. Glaciol. **15**, 81 (1991).
[13] M. van den Berg, R. Lubbad, and S. Løset, Cold Reg. Sci. Technol. **155**, 193 (2018).
[14] J. Ranta and A. Polojärvi, Mar. Struct. **67**, 102633 (2019).
[15] M. Prasanna, M. Wei, A. Polojärvi, and D. Cole, Cold Reg. Sci. Technol. **189**, 103315 (2021).
[16] J. Åström, Adv. Phys. **55**, 247 (2006).
[17] J. Åström, T. Riikilä, T. Tallinen, T. Zwinger, D. Benn, J. Moore, and J. Timonen, Cryosphere **7**, 1591 (2013).
[18] J. Todd, J. Åström, and D. I. Benn, The Helsinki discrete element model (HiDEM), https://github.com/joeatodd/HiDEM.git (2018).
[19] D. Potyondy and P. Cundall, Int. J. Rock Mech. Mining Sci. **41**, 1329 (2004).
[20] H. A. Carmona, F. K. Wittel, F. Kun, and H. J. Herrmann, Phys. Rev. E **77**, 051302 (2008).
[21] F. Kun, I. Varga, S. Lennartz-Sassinek, and I. G. Main, Phys. Rev. E **88**, 062207 (2013).
[22] F. Kun, I. Varga, S. Lennartz-Sassinek, and I. G. Main, Phys. Rev. Lett. **112**, 065501 (2014).
[23] G. Timár, J. Blömer, F. Kun, and H. J. Herrmann, Phys. Rev. Lett. **104**, 095502 (2010).
[24] T. Riikilä, T. Tallinen, J. Åström, and J. Timonen, Comput. Phys. Commun. **195**, 14 (2015).
[25] H. A. Carmona, F. Kun, J. S. Andrade, and H. J. Herrmann, Phys. Rev. E **75**, 046115 (2007).
[26] S. Lennartz-Sassinek, I. G. Main, Z. Danku, and F. Kun, Phys. Rev. E **88**, 032802 (2013).
[27] M. Jirásek and Z. Bažant, J. Eng. Mech. **121**, 1016 (1995).
[28] D. André, B. Levraut, N. Tessier-Doyen, and M. Huger, Comput. Methods Appl. Mech. Eng. **318**, 898 (2017).
[29] Z. Xu, A. M. Tartakovsky, and W. Pan, Phys. Rev. E **85**, 016703 (2012).
[30] A. Herman, Geosci. Model Dev. **9**, 1219 (2016).
[31] A. Herman, Cryosphere **11**, 2711 (2017).
[32] A. Damsgaard, O. Sergienko, and A. Adcroft, J. Adv. Model. Earth Syst. **13**, e2020MS002336 (2021).
[33] N. Golding, E. Schulson, and C. Renshaw, Acta Mater. **58**, 5043 (2010).
[34] D. I. Benn and J. A. Åström, Adv. Phys.: X **3**, 1513819 (2018).
[35] D. Benn, J. Åström, T. Zwinger, J. Todd, F. Nick, S. Cook, N. Hulton, and A. Luckman, J. Glaciol. **63**, 691 (2017).
[36] E. van Dongen, J. Åström, G. Jouvet, J. Todd, D. Benn, and M. Funk, Front. Earth Sci. **8**, 253 (2020).
[37] S. Cook, J. Åström, T. Zwinger, B. Keith Galton-Fenzi, J. Stevens Greenbaum, and R. Coleman, Cryosphere **12**, 2401 (2018).
[38] J. Åström and D. Benn, Geophys. Res. Lett. **46**, 13099 (2019).
[39] J. Paavilainen, J. Tuhkuri, and A. Polojärvi, Eng. Comput. **26**, 578 (2009).
[40] A. Hillerborg, M. Modéer, and P.-E. Petersson, Cem. Concr. Res. **6**, 773 (1976).
[41] K.-J. Bathe, *Finite Element Procedures* (Prentice Hall, Englewood Cliffs, NJ, 1996).
[42] W. Weeks and W. D. Hibler, *On Sea Ice*, 1st ed. (University of Alaska Press, Fairbanks, 2010).
[43] B. Yang, Y. Jiao, and S. Lei, Eng. Comput. **23**, 607 (2006).
[44] T.-T. Nguyen, D. André, and M. Huger, Comput. Particle Mech. **6**, 393 (2019).
[45] E. M. Schulson and O. Y. Nickolayev, J. Geophys. Res. **100**, 22383 (1995).
[46] M. Thouless, A. Evans, M. Ashby, and J. Hutchinson, Acta Metall. **35**, 1333 (1987).
[47] M. Zhou, Proc. Roy. Soc. A: Math. Phys. Eng. Sci. **459**, 2347 (2003).
[48] E. M. Schulson, A. L. Fortt, D. Iliescu, and C. E. Renshaw, J. Geophys. Res.: Oceans **111**, C11S25 (2006).
[49] J. Weiss, V. Pellissier, D. Marsan, L. Arnaud, and F. Renard, J. Geophys. Res.: Solid Earth **121**, 8523 (2016).
[50] E. Schulson, A. Fortt, D. Iliescu, and C. Renshaw, Acta Mater. **54**, 3923 (2006).
[51] See Supplemental Material at http://link.aps.org/supplemental/10.1103/PhysRevE.105.045001 for the results of length-scale analysis.
[52] J. Weiss, L. Girard, F. Gimbert, D. Amitrano, and D. Vandembroucq, Proc. Nat. Acad. Sci. USA **111**, 6231 (2014).
[53] J. Weiss and E. Schulson, J. Phys. D **42**, 214017 (2009).